PCCP

Accepted Manuscript




ROYAL SOCIETY OF CHEMISTRY

www.rsc.org/pccp

Journal Name

Cite this: DOI: 10.1039/c0xx00000x

www.rsc.org/xxxxxx

ARTICLE TYPE

# Synergy between molybdenum nitride and gold leading to platinum-like activity for hydrogen evolution

**Adina Morozan,[a] Vincent Goellner,[a] Andrea Zitolo,[b] Emiliano Fonda,[b] Bruno Donnadieu,[a] Deborah Jones[a] and Frédéric Jaouen *[a]**

***Received (in XXX, XXX) Xth XXXXXXXXX 20XX, Accepted Xth XXXXXXXXX 20XX***
**DOI: 10.1039/b000000x**

Reduced size and direct electrochemical $H_2$ compression are two distinct advantages of electrolyzers based on the acid-polymer electrolyte membrane technology over those relying on alkaline electrolytes. However, recourse to catalysts based on the scarce platinum-group-metals has hitherto been the price to pay. While transition metal sulfides and nitrides of group VI have recently shown interesting activities for $H_2$ evolution, the remaining activity gap with Pt needs to be reduced. Platinum owes its high activity to its optimum metal-hydrogen bond strength for $H_2$ evolution, which is a proven descriptor of the activity on single-component catalysts. Here, we unravel a major synergetic effect between gold and molybdenum nitride which multiplies the hydrogen evolution activity *ca* 100 times over that of either gold or molybdenum nitride. This two-phase catalytic material, featuring both strong and weak metal-hydrogen bonds, overcomes the limitations described by Sabatier's principle for single-component catalysts.

## Introduction

While solar and wind energies could in principle satisfy the lion's share of the global energy demand,[1] their integration in the power grid is challenged by intermittent power production. Electrolyzers can be used to reversibly store such electrical energy in the form of dihydrogen.[2] Alkaline and proton-exchange membrane (PEM) electrolyzers are appropriate for intermittent $H_2$ production, even though both require electrocatalysts to reach a high efficiency. PEM electrolyzers, owing to the solid polymer-electrolyte membrane, offer the advantages of delivering electrochemically pressurized ultra-pure $H_2$ at very high current densities.[3,4]

Even though the cathodic hydrogen evolution reaction (HER) in acid medium is facile on platinum-group metals (PGMs),[5-6] a large-scale deployment of PEM electrolyzers would require significant amounts of such metals. Beside the cost issue, limited supply of PGMs is a strong incentive to search for alternative catalysts. In this respect, transition metal carbides and nitrides of group VI have attracted much interest.[7-10] Regarding the HER in acid medium, the earliest reports featured bio-inspired molybdenum sulfides as synthetic analogues of the FeMo-cofactor in nitrogenase enzyme.[11,12] Later, $MoS_2$ nanostructures with many edge sites showed improved activity.[12-17] Molybdenum boride and carbide have also shown high HER activity in basic and acid media,[18-20] paralleling the attractive activity and stability in acid medium of W- or Mo-nitrides.[21,22] Mo- or W-based carbides, nitrides and sulfides are however still less active for the HER than PGMs. The latter owe their high intrinsic activity to an appropriate metal-hydrogen (M-H) bond strength for this reaction.[5,23] Another approach for designing HER catalysts has involved combining elements having a higher M-H bond strength than PGMs, *e.g.* Mo, with elements having a lower M-H bond strength, *e.g.* Ni, each element being selected to catalyze a targeted step of the HER. Examples based on this approach comprise the Ni(Co)Mo alloys,[24,25] and recently $NiMoN_x$ binary metal nitrides with higher stability in acid medium.[21] In this approach, gold is an interesting element to combine with Mo due to its weak bonding of hydrogen adatoms.[5,23,26] In this work, we report on a major synergetic effect between γ-$Mo_2N$ nanoparticles and gold, leading to improved HER activity in acid medium. The best Au/$Mo_2N$/C catalyst showed a 170-200 mV positive shift relative to both Au/C and $Mo_2N$/C and trailed the polarisation curve of a 70 wt. % Pt/C catalyst by only 30 mV at 1 mA·cm$^{-2}$. The HER on Au/$Mo_2N$/C likely proceeds with the first electron transfer occurring on γ-$Mo_2N$, followed by surface diffusion of hydrogen adatoms to gold atoms or particles where $H_2$ is rapidly evolved *via* the Tafel or Heyrovski pathway.

## Experimental

### Catalyst synthesis

We used the $Zn^{II}$ zeolitic imidazolate framework ($ZnN_4C_8H_{12}$, Basolite Z1200, labelled Z8), furfuryl alcohol (FA), $Mo^{II}$ acetate ($Mo^{II}Ac$) and 1,10-phenanthroline (phen). Z8 was impregnated with FA. The resultant mixture was stirred for 24 h, filtered and washed with mesitylene to remove excess FA. The resulting powder was labelled Z8FA. We then prepared Mo/phen/Z8FA catalyst precursors of weight compositions 3/20/80 and 6/20/80 ($m_{Z8FA}$ = 800, $m_{phen}$ = 200, $m_{MoAc}$ = 69 and 138 mg, respectively). The suspension was stirred, then slowly evaporated and dried at 80ºC overnight. The dry powder was then ball-milled in a

zirconium oxide crucible filled with 100 zirconium oxide balls of 5 mm diameter to form the catalyst precursor. The vial was sealed under air and placed in a planetary ball-miller to undergo 4 cycles of 30 min of ball-milling at 400 rpm. The catalyst precursor was then placed in the oven and ramp-heated (5 ºC·min$^{-1}$) under flowing Ar to 1050 ºC and held at this temperature for 1 h. A reference Mo-free N-doped carbon was also synthesized according to the same procedure. The nomenclature to identify the catalysts is as follows: MoA/B/C-Z8FA-1050, where A is the weight percentage of Mo in the catalyst precursor, B/C the mass ratio of phen/Z8FA and 1050 the temperature of pyrolysis in Ar.

**Physico-chemical characterization**

High Resolution TEM experiments were performed on a I2TEM (HF 3300C) Cs corrected microscope working at 200kV. Samples were also investigated with scanning transmission electron microscopy on a JEM-2200FS microscope. X-ray diffraction was conducted using a PANanalytical X'Pert Pro powder X-ray diffractometer. Mo K-edge XANES and EXAFS spectra were recorded at room temperature in transmission mode at the SAMBA beamline of the SOLEIL synchrotron.[27] The EXAFS data analysis was performed with the GNXAS code which is based on the theoretical calculation of the X-ray absorption fine structure signal and a subsequent refinement of the structural parameters. In the GNXAS approach, the interpretation of the experimental data comprises the decomposition of the $\chi(k)$ signal into a summation over n-body distribution functions $\gamma^{(n)}$ calculated by means of the MS theory.[28,29] XPS spectra were recorded with a Physical Electronics PHI 5701 spectrometer. Non-monochromatic Mg $K_\alpha$ X-ray was used as the excitation source. Fitting of the $Mo_{3d}$ spectrum involved three Mo species and hence 6 apparent peaks due to spin splitting. The constraints applied to the $Mo_{3d}$ fitting were i) 5/2 to 3/2 peak-to-peak separation of 3.13 eV and ii) $Mo3d_{3/2}$ to $Mo3d_{5/2}$ area ratio of 2/3.

**Rotating-disk electrode measurements**

A saturated calomel electrode (SCE) was used as a reference electrode, and unless otherwise stated a gold wire (0.5 mm diameter, 99.95 % pure) as a counter electrode. The SCE was calibrated against a reversible hydrogen electrode (RHE). For the Mo/N/C or N/C catalysts, the ink contained 10 mg of catalyst, 95 µl of a 5 wt.% Nafion® solution and 350 µl of ethanol. Next, an aliquot of 7 µl was deposited onto the glassy carbon disk, leading to a loading of 800 $\mu g_{Mo/N/C} \cdot cm^{-2}$. A Pt/C catalyst (Tanaka, 70 wt% Pt/C, 3 nm Pt particles) was used as a reference. The ink for Pt/C included 5 mg of catalyst, 20 µL of a 5 wt. % Nafion® solution, 242 µL ethanol and 10 µL $H_2O$. An aliquot of 5 µl was deposited on the glassy-carbon disk, resulting in a loading of 328 $\mu g_{Pt} \cdot cm^{-2}$. The HER polarization curve was measured at 1500 rpm and at a scan rate of 1 $mV \cdot s^{-1}$ in a $N_2$-saturated electrolyte. All curves are compensated for the ohmic drop.

## Results and discussion

**Characterization of pristine catalysts**

The catalysts Mo3/20/80-Z8FA-1050 and Mo6/20/80-Z8FA-1050 were synthesized according to the method described in the experimental section. The mass loss during pyrolysis was 68-70 wt. % due to C, N and Zn volatile products formed during the transformation of Z8FA and phen into a high surface-area carbon material.[30] This resulted in *ca* 9 and 20 wt. % Mo contents in the final catalysts derived from the 3 and 6 wt. % Mo precursors, respectively. Figure 1a shows the X-ray diffraction patterns for these two Mo-based catalysts. All peaks could be assigned to graphite and γ-$Mo_2N$. However, the diffraction peak at *ca* 42.5° results from the superimposition of the 101 graphite and 200 γ-$Mo_2N$ reflections. The average size of the $Mo_2N$ crystals is identical in both catalysts, 15.4-16.8 Å, as determined from the Scherrer equation. In γ-$Mo_2N$, molybdenum atoms define a face-centered cubic structure while nitrogen atoms randomly occupy half of the interstitial octahedral sites.[31] The square arrangement of Mo atoms was confirmed by TEM (Fig.1b). The particle size observed with TEM is similar to the average crystal size determined with XRD, suggesting that particles are single crystals. Noteworthy, assuming a cubic shape, a particle size of 16.6 Å corresponds to edges involving only 5 Mo atoms separated by a Mo-Mo distance of 4.16 Å, the unit-cell parameter of γ-$Mo_2N$. Such a cube with *fcc* structure contains 365 Mo atoms, of which 194 (*ca* 50 %.) sit on the top-surface. On a mesoscopic scale, the distribution of Mo, N and O-atoms is uniform (Fig.1-c-d-e). While N and O hetero-atoms from the carbon support also contribute to the STEM signal, the match between the signal intensities of Mo, N and O suggests that the majority of N and O-atoms are located in or on γ-$Mo_2N$ particles.

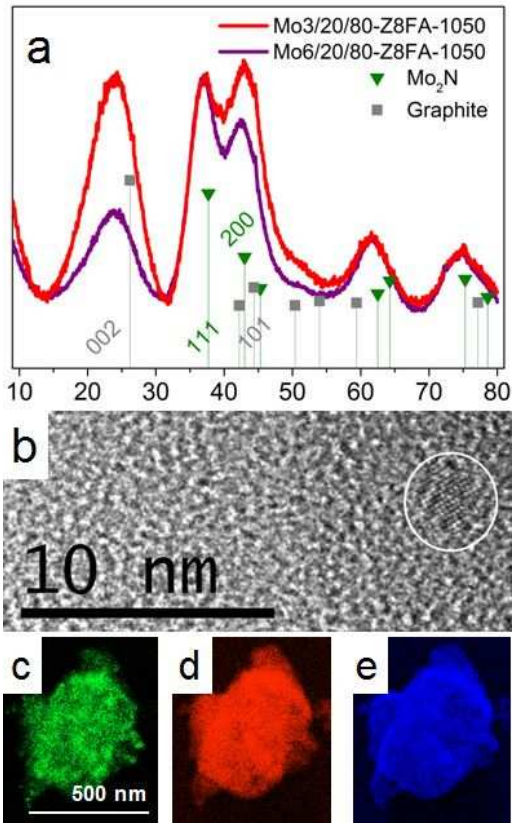


Fig. 1. Structural characterization of pristine catalysts . a) Powder X-ray diffractograms measured with the Cu $K_\alpha$ radiation and reference X-ray diffraction lines for γ-$Mo_2N$ (JCPDS file 25-1366) and graphite (JCPDS file 75-1621), b) High-resolution TEM image of Mo3/20/80-Z8FA-1050 showing a molybdenum nitride nanoparticle with cubic ordering of the Mo atoms on the disordered N-doped carbon support, c-d-e) STEM mapping on a single catalytic particle for Mo, N and O, respectively.

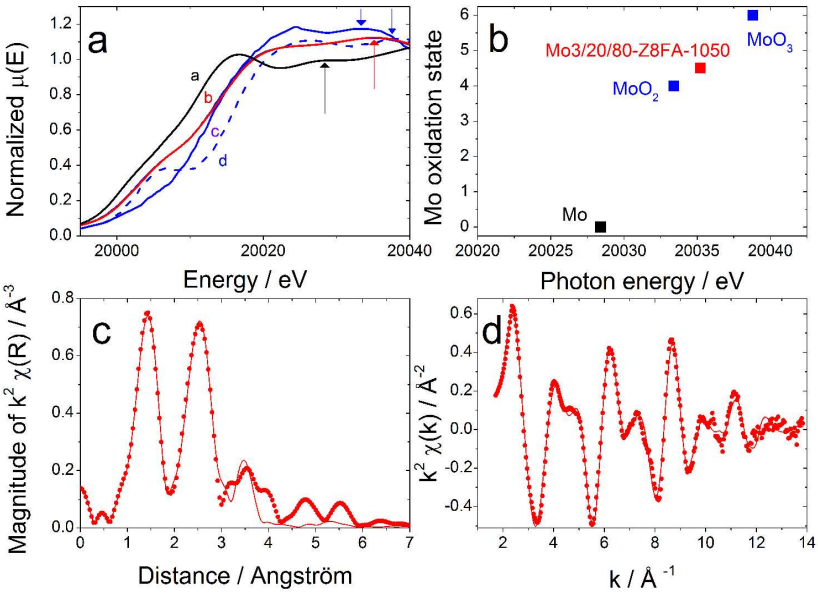


Figure 2. X-ray absorption characterization. a) K-edge XANES spectra of a) the reference Mo-foil, b) Mo3/20/80-Z8FA-1050, c) $MoO_2$ , d) $MoO_3$ (oxides digitalized from Ref. 32), b) Correlation between the Mo oxidation state and the position of the second peak in the XANES spectra (indicated by the arrows in panel a), c) Magnitude of the $k^2$-weighed Fourier transform of the EXAFS signal for Mo3/20/80-Z8FA-1050 (dots) and its fitting (solid line), d) $k^2$-weighed EXAFS function for Mo3/20/80-Z8FA-1050 and its fitting (solid line).

Next, the X-ray absorption near-edge structure (XANES) and extended X-ray absorption fine structure (EXAFS) spectra were recorded on Mo3/20/80-Z8FA-1050 (Fig. 2). The correlation between the Mo K-edge position and oxidation state [32] enabled us to determine an average oxidation state of 4.5 for Mo atoms (Fig. 2b). The Fourier-transform radial distribution function (Fig. 2c) shows a first peak arising from Mo-N and/or Mo-O interactions, and a second and third peak assigned to backscattering from Mo atoms. Structural parameters of the first coordination sphere obtained from EXAFS fitting matched those of γ-$Mo_2N$ (supplementary Table S1). However, to improve the agreement between the calculated and experimental spectra, an additional short Mo-O bond was required. The fitted value of 1.77 Å is typical for Mo-O bond lengths.[33] The average coordination number for Mo-Mo in the second coordination sphere is only 4.7, instead of 12 for bulk $Mo_2N$. This is due to the large fraction of surface Mo atoms with low coordination. On the other hand, the average coordination number of 4.0 for Mo-N suggests that the $Mo_2N$ structure is terminated with N-atoms on the surface. Moreover, the average coordination number of *ca* 1.5 assigned to Mo-O suggests that the surface layer is oxygen-rich, which was previously indicated by STEM (Fig. 1e).[34]

The Mo oxidation state and O-content in Mo3/20/80-Z8FA-1050 and Mo6/20/80-Z8FA-1050 were further investigated with X-ray photoelectron spectroscopy (XPS), supplementary Fig.S1. Deconvolution of the $Mo_{3d}$ spectra involved three species resulting in six apparent peaks due to spin-splitting. Binding energies (BE) of 228.8, 229.9 and 232.5 eV for the $Mo3d_{5/2}$ level were assigned to $Mo^{\delta}$ ($1.5 < \delta < 3$), $Mo^{IV}$ and $Mo^{VI}$, respectively (supplementary Table S2).[35] The $Mo_{3d}$ spectrum resembles that previously reported for passivated $Mo_2N$ nanoparticles.[36] Next, the $O_{1s}$ narrow scan spectra were deconvoluted with three BE of 530.8, 532.6 and 534.4 eV. They are assigned to metal-bound oxygen, C=O groups on carbon or adventitious oxygen[37,38] and C-O-H or C-O-C groups,[37] respectively. With 40-60% of the O-atoms bound to Mo in the two catalysts, the XPS data support the presence of oxygen in the $Mo_2N$ particles, which was previously inferred from the STEM-mapping and from EXAFS fittings.

**Electrochemical activity for $H_2$ evolution**

Figure 3 shows polarization curves for the HER before/after 1000 electrochemical cycles from -0.6 to +0.4 V *vs.* a saturated calomel electrode (SCE). Both Mo3/20/80-Z8FA-1050 and Mo6/20/80-Z8FA-1050 show a major improvement in HER activity after the cycling (Fig.3a, arrows), but the improvement is even larger for Mo6/20/80-Z8FA-1050. For the measurements reported in Fig. 3a, a gold wire was used as a counter electrode (CE) during the electrochemical cycling. In order to provide evidence for the gold promotion during cycling, the gold wire was replaced by a graphite rod for another series of measurements. Figure 3b reports the HER activity before and after cycling Mo3/20/80-Z8FA-1050, when using a graphite rod as a CE. Here, a negligible activity enhancement was observed on Mo3/20/80-Z8-1050, thereby demonstrating the role played by gold for the activity enhancement during cycling. A second test experiment was designed in order to identify whether the high activity observed after cycling might be due to gold alone. The N-doped carbon obtained from the pyrolysis of Z8FA and phen was selected for that purpose (Mo0/20/80-Z8FA-1050). Figure 3c shows that some activity enhancement was also observed on Mo0/20/80-Z8FA-1050. However, the final HER activity (potential at -1 mA $cm^{-2}$) after cycling is 100 and 200 mV below that of Mo3/20/80-Z8FA-1050 and Mo6/20/80-Z8FA-1050, respectively (Fig. 3a). Hence, electrochemical activation of $Mo_2N$

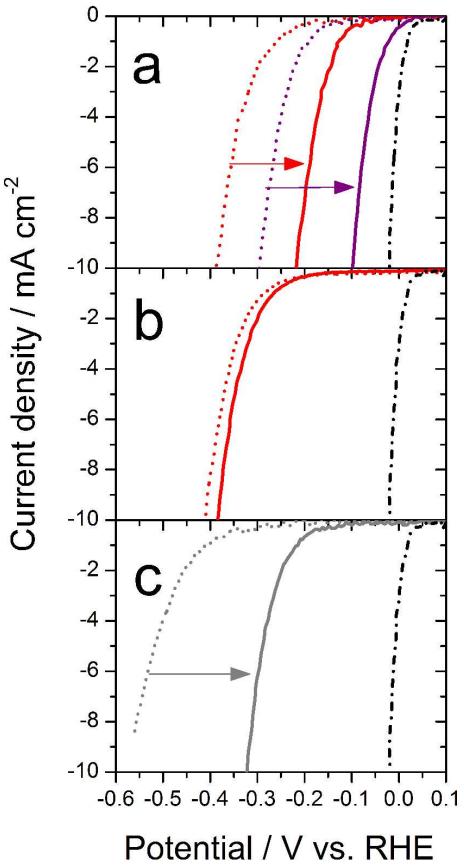


Figure 3. Hydrogen evolution reaction on Mo-based catalysts and N-doped carbon. Polarization curves before and after electrochemical cycling (short dashed lines and solid lines, respectively) for a) Mo3/20/80-Z8FA-1050 (red) and Mo6/20/80-Z8FA-1050 (purple); gold counter electrode, b) Mo3/20/80-Z8FA-1050; graphite counter electrode, c) Mo0/20/80-Z8FA-1050; gold counter electrode. 0.1 M $H_2SO_4$ electrolyte, scan rate 1 mV $s^{-1}$, rotating speed 1500 rpm, catalyst loading 800 $\mu g_{Mo/N/C}$ $cm^{-2}$, 1000 cycles were performed at 100 mV $s^{-1}$ from -0.6 to +0.4 V *vs.* SCE (-0.29 to + 0.71 V *vs.* RHE). The reference Pt/C catalyst (dot-dash-dot line) is a commercial 70% Pt/C catalyst (Tanaka) measured in 0.1 M $HClO_4$ solution, loading 328 $\mu g_{Pt}$ $cm^{-2}$

nanoparticles with gold explains the high HER activity observed after cycling (Fig. 3a). Promotion by gold is understandable if the gold CE releases metal cations subsequently electrodeposited on the working electrode (WE). Indeed, when the WE is polarized between -0.6 and +0.4 V *vs.* SCE (-0.29 to + 0.71 V *vs.* RHE), the reduction current generated during the cathodic polarization imposes an oxidation current at the CE. The main oxidation current at the gold CE is gold anodic dissolution. Gold cations released in the electrolyte are then electro-reduced at the WE since the entire range of potential imposed on the WE during cycling is below the equilibrium potential for $Au^{3+}/Au$, 1.53 V *vs.* NHE. The process by which the metal from the CE is re-deposited at the WE has previously been applied to investigate the effect of Pt-on-Au for the HER activity.[39] In the present case, the condition sufficient for gold electro-deposition during cycling of the WE is $E_{low} < E_{onset}$, where $E_{low}$ is the lowest potential of the WE during cycling and $E_{onset}$ the onset potential of the HER at the WE. If $E_{low} > E_{onset}$, the WE never generates a reduction current during cycling. Indeed, no activity enhancement occurred with Mo6/20/80-Z8FA-1050 when using a gold CE if $E_{low}$ was raised

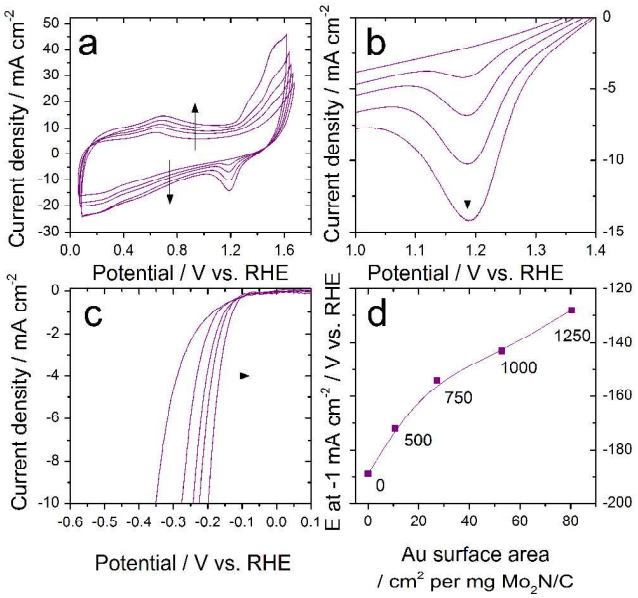


Figure 4. Electrochemical identification of gold *vs.* the number of activation cycles (0, 500, 750, 1000, 1250 cycles). a) 50 mV $s^{-1}$ gold-identification voltammetry on Mo6/20/80-Z8FA-1050 *vs* cycle number, b) Reduction peak assigned to a gold-oxide monolayer (zoom of panel A) *vs* cycle number, c) HER polarization curve measured at 1 mV $s^{-1}$ *vs* cycle number, d) HER activity as a function of the gold surface area. Data points are labelled by their corresponding cycle number. 0.1 M $H_2SO_4$ electrolyte, 1500 rpm rotation, catalyst loading 800 $\mu g_{Mo/N/C}$ $cm^{-2}$. Cycling was performed at 100 mV $s^{-1}$ from -0.29 to + 0.71 V *vs.* RHE for 500 cycles, then by steps of 250 additional cycles, without changing the electrolyte. All other experiments were performed in fresh electrolyte. Arrows indicate trends with increased cycling number.

from -0.29 to +0.17 V *vs.* RHE (supplementary Fig.S2a). The HER activity can be conveniently quantified with the electric potential necessary to reach -1 mA $cm^{-2}$. With that definition, the HER activity of Mo3/20/80-Z8FA-1050 before cycling is -260 mV *vs.* RHE, similar to that reported by Adzic's group for δ-MoN/Vulcan.[21] The activity of Mo6/20/80-Z8FA-1050 increased from -205 to -20 mV *vs.* RHE during 1000 cycles. The latter activity is only 30 mV below that for 70 wt. % Pt/C (Fig.3) and higher than any previously reported HER activity for Mo-based or non-PGM catalysts (supplementary Table S3). While being a precious metal, gold does not belong to PGMs and its average production worldwide is 14 times larger than that of Pt.

**Characterization of gold-promoted $Mo_2N$/C catalysts**

Following this preliminary understanding, the presence of gold after cycling was verified electrochemically. Using a gold CE, Mo6/20/80-Z8FA-1050 was activated in the potential range -0.29 to + 0.71 V *vs.* RHE. After 500 such cycles, the WE was transferred to a clean electrolyte and a new HER polarisation curve was recorded at 1 mV·$s^{-1}$ while voltammetry in the range of 0.0 to 1.75 V *vs.* RHE was performed at 50 mV·$s^{-1}$. The latter voltammetry captures redox peaks characteristic of oxidation of a monolayer of the gold surface to AuO (1.2-1.6 V *vs.* RHE) and its reversible reduction (0.85-1.25 V *vs.* RHE).[26] Figure 4a shows such voltammograms after 0, 500, 750, 1000 and 1250 activation cycles. The initial voltammogram does not show any gold peak and the broad redox peak at 0.3/0.7 V *vs.* RHE is assigned to passivated $Mo_2N$. After 500 activation cycles, a well-defined

peak assigned to gold reduction is observed at 1.18 V *vs.* RHE (Fig. 4b), while the oxidation peaks at 1.33 and 1.5 V *vs.* RHE are poorly defined compared to those observed on pure Au surfaces.[26] From the charge below the Au-reduction peak (Fig.4b) and the charge of 390 μC $cm^{-2}$ known for polycrystalline gold,[40] the gold surface area could be estimated. As shown in Fig.4d, it is positively correlated with the increase in HER activity.

The spatial distribution of electrodeposited gold and the hypothetical existence of Mo-Au bonds were then investigated with STEM and EXAFS (Fig. 5). The catalyst Mo6/20/80-Z8FA-1050 after 500 cycles shows a homogeneous distribution of molybdenum and gold atoms on the N-doped carbon support (Fig. 5a-b). While informative, the STEM image does not allow us to conclude on the existence or absence of Mo-Au bonds. This was further investigated with EXAFS. The EXAFS signal at the Mo K-edge could be fitted without any contribution from Mo-Au interactions (Fig. 5c and supplementary Table S1), while XANES at the Au L3-edge is identical to that of a gold foil (Fig. 5d). In conclusion, the X-ray absorption data on the cycled Mo6/20/80-Z8FA-1050 catalyst shows that gold atoms are present as gold nanoparticles, and atomic Mo-Au bonds are not detected. Thus, the observed HER activity enhancement after cycling likely arises from a short average distance between $Mo_2N$ and gold nanoparticles, enabling a synergetic catalytic effect toward the HER. This hypothesis also explains the larger improvement in HER activity observed for Mo6/20/80-Z8FA-1050 than for Mo3/20/80-Z8FA-1050 (Fig.3a). Both the higher Mo loading and the lower specific surface area of the N-doped carbon in the former catalyst (454 *vs.* 705 $m^2g^{-1}$) likely result in a shorter average distance between $Mo_2N$ and Au particles after cycling.

In order to estimate the average size of the electrodeposited gold particles, TEM images of Mo6/20/80-Z8FA-1050 were recorded after 500 and 1000 cycles (Fig. 6). In Fig. 6a, the nanoparticle size is monodisperse, suggesting that the Au nanoparticles deposited after 500 cycles have an average size similar to that of the $Mo_2N$ nanoparticles, *ca* 2 nm. In contrast, after 1000 cycles, gold spherical particles about 20 nm in size are observed while $Mo_2N$ rafts *ca* 2.0 nm in size are still visible on HR-TEM images (not shown). Thus, the size of the electrodeposited gold particles increases with increased cycling. This explains the shape of the plot of activity *vs* gold area (Fig.4d). Initially gold is deposited as 2 nm particles, and the average distance between $Mo_2N$ and Au particles strongly decreases (0-750 cycles). In a second stage, gold electrodeposition occurs mainly on pre-existing gold particles, which affects less the average distance between $Mo_2N$ and Au particles. Consequently the increase in HER activity is slowed down (> 750 cycles, Fig.4d). Last, from the average Au particle size of 20 nm after 1000 cycles and from the gold area (*ca* 50 $cm^2/mg_{MoNC}$ after 1000 cycles, Fig. 4d), we estimated the gold loading to be 254 μg $cm^{-2}$ after 1000 cycles. This is slightly less than the Pt loading used for the Pt curve in Fig. 3, 328 $\mu g_{Pt}$ $cm^{-2}$. From these loadings and assuming the Au and Pt nanoparticles to be spherical with respective diameters of 20 and 3 nm, the geometric current density could be converted into a surface specific activity. From Figure S3a, the surface specific activities at -0.05 V vs. RHE were found to be 0.06 mA $cm^{-2}_{Au}$ and 0.086 mA $cm^{-2}_{Pt}$ for Au/$Mo_2N$/C and Pt/C, respectively.

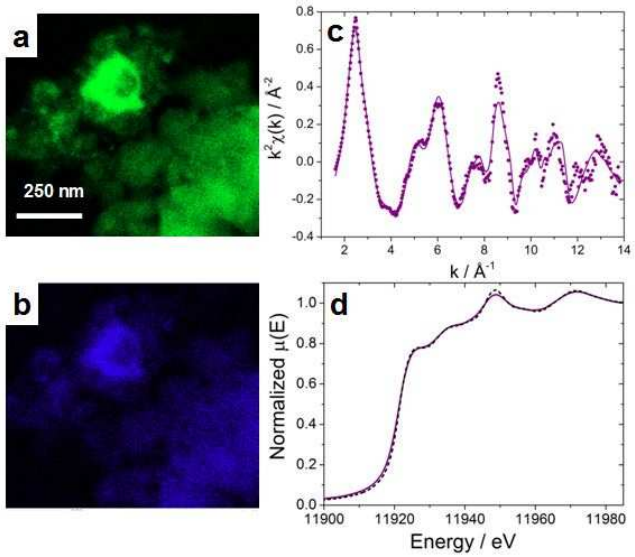


Figure 5. Microscopic and spectroscopic identifications of Mo and Au in Mo6/20/80-Z8FA-1050 after 500 cycles. a) STEM mapping for Mo in Mo6/20/80-Z8FA-1050, b) STEM mapping for Au in Mo6/20/80-Z8FA-1050, c) $k^2$-weighed EXAFS function at the Mo K-edge (circles) and its fitting (solid line), d) XANES spectra at the Au L3-edge for a gold foil (dashed line) and for Mo6/20/80-Z8FA-1050 (solid purple line). 0.1 M $H_2SO_4$ electrolyte, rotating speed 1500 rpm, catalyst loading 800 $\mu g_{Mo/N/C}$ $cm^{-2}$. The cycling was performed at 100 mV $s^{-1}$ from -0.6 to +0.4 V *vs.* SCE for 500 cycles and using a gold counter electrode.

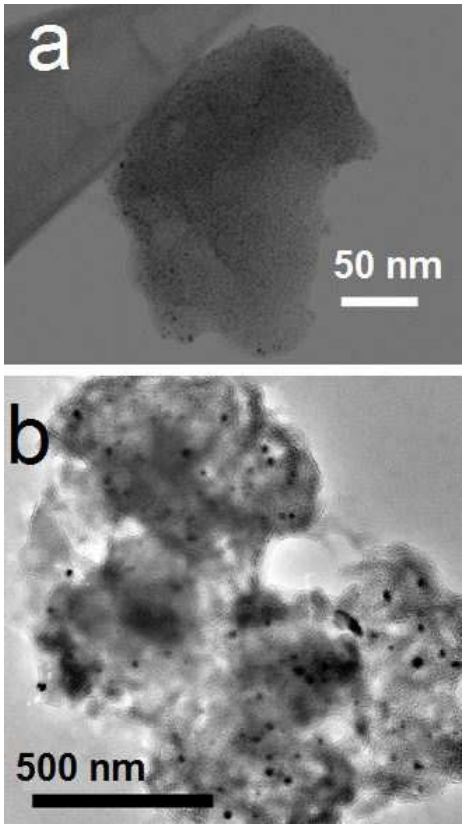


Figure 6. TEM image of Mo6/20/80-Z8FA-1050 after a) 500 cycles, b) 1000 cycles. The catalyst was cycled at 100 mV $s^{-1}$ from -0.6 to +0.4 V *vs.* SCE in 0.1 M $H_2SO_4$, rotation 1500 rpm, gold counter electrode.

**Hydrogen evolution mechanism**

To discuss the HER mechanism, we adhere to the formalism for multistep electrochemical reactions reported by Fletcher.[41] The elementary steps are:

| | | |
|---|---|---|
| $H_3O^+ \rightarrow H^+_{ads} + H_2O$ | Adsorption | (1) |
| $H^+_{ads} + e \rightarrow H^\bullet_{ads}$ | Volmer | (2) |
| $H^\bullet_{ads} \rightarrow H^\bullet_{ads}$ | Diffusion | (3) |
| $2\ H^\bullet_{ads} \rightarrow H_2$ | Tafel | (4) |
| $H^\bullet_{ads} + H_3O^+ + e \rightarrow H_2 + H_2O$ | Heyrovski | (5) |

The reaction may proceed according to the reaction path 1-2-4 or 1-2-5, known as the Volmer-Tafel and Volmer-Heyrovski mechanisms. The diffusion step 3 shows the possibility for hydrogen adatoms to diffuse from one type of surface to another. In each of the two mechanisms, either the first electron transfer (2) or the following step (4 or 5) may be the rate-determining step (rds). This predicts Tafel slopes of 120/(1-Δ) mV·dec.$^{-1}$ if (2) is the rds, 30 mV·dec.$^{-1}$ if (4) is the rds and 120/(3-Δ) mV·dec.$^{-1}$ if (5) is the rds; with Δ defined by $\beta = 0.5x(1-\Delta)$ where β is the cathodic symmetry factor of the electron transfer during the rds. In general, Δ is within the range ± 0.2. The Tafel slopes of the Mo-based catalysts after gold electro-deposition are in the range of -78 to -67 mV·dec.$^{-1}$ (Fig.S3a). These experimental slopes do not correspond to any of the above predicted Tafel slopes. This mismatch can be explained if the diffusion step (3) is the rds. It is proposed that reactions (1-2) occur on the $Mo_2N$ surface, followed by the diffusion of hydrogen adatoms to the nearest gold atom or surface where either reaction (4) or (5) closes the HER mechanism. This mechanism leads to a theoretical Tafel slope of 60 mV·dec.$^{-1}$ if (3) is the rds.[41] This mechanism has been recognized in various instances[42,43] and is in agreement with the experimentally measured Tafel slopes of the most active catalysts of the present work. It also explains the match between the HER onset potential on Au/$Mo_2N$/C and the onset potential for the hydrogen electrochemical adsorption on $Mo_2N$ (Fig.S2d). The synergetic effect of Au and $Mo_2N$ may also explain the recently reported enhanced HER activity (+50 mV) for $MoS_2$ or $WS_2$ following their decoration with Au-nanoparticles[44] or deposition on a gold surface.[45] It may also explain the higher turnover frequency for $MoS_2$ nanostructures deposited on Au(111) relative to other $MoS_2$ nanostructures.[14,46] In the present work on $Mo_2N$ however, the magnitude of activity enhancement due to gold is much larger (+180 mV).

## Conclusion

Tremendous synergy between gold and $Mo_2N$ particles for the HER is reported, leading to the best HER activity in acid medium reported so far for both non-PGM catalysts and gold-promoted non-PGM catalysts. The synergy arises from the combination of $Mo_2N$ strongly binding hydrogen with Au, having a low affinity for hydrogen atoms. This combination overcomes the non-optimum metal-hydrogen bonding energy intrinsic to Mo and Au, as is visible on the volcano plot reflecting Sabatier's principle. While gold is a precious metal, its production in 2013 was 14 times that of platinum and also more widespread geographically. Replacing platinum by gold for the HER in acid medium would therefore be beneficial from a resources viewpoint. Ideally, catalysts free of any precious metals and with Pt-like activity need to be developped and tested in PEM electrolyzers. The present example of strong synergetic effect may be sought for non-precious metal catalysts as well.

## Acknowledgements

We acknowledge funding by ANR under contract 2011 CHEX 004 01. The authors acknowledge the French network METSA funded by the CNRS for HR-TEM measurement.

## Notes and references

[a] *Institut Charles Gerhardt de Montpellier - UMR 5253, Place Eugène Bataillon, 34095 Montpellier cedex 5, France.*
*Tel: +33 467143211; E-mail: frederic.jaouen@univ-montp2.fr*
[b] *Synchrotron SOLEIL*
*L'Orme des Merisiers Saint-Aubin - BP 48*
*91192 Gif-sur-Yvette, France*

† Electronic Supplementary Information (ESI) available: parameters from EXAFS fitting for pristine and gold-promoted catalysts, narrow scan spectra and elemental content from XPS, table of HER activity, effect of the lower-potential limit on activation, Tafel plots corresponding to Fig. 3. See DOI: 10.1039/b000000x/

1 P. C. K. Vesborg and T. F. Jaramillo, *RSC Adv.*, 2012, **2,** 7933-7947.
2 J. D. Holladay, J. Hu, D. L. King and Y. Wang, *Catal. Today*, 2009, **139,** 244-260.
3 M. Carmo, D. L. Fritz, J. Mergel and D. A. Stolten, *Int. J. Hydrogen Energy*, 2013, **38,** 4901-4934.
4 S. A. Grigor'ev, M. M. Khaliullin, N. V. Kuleshov and V. N. Fateev, *Russ. J. Electrochem.*, 2001, **37,** 819-822.
5 J. K. Norskov T. Bligaard, A. Logadottir, J. R. Kitchin, J. G. Chen, S. Pandelov and U. Stimming *J. Electrochem. Soc.*, 2005, **152,** J23-J26.
6 P. Millet, R. Ngameni, S. S. Grigoriev, N. Mbemba, F. Brisset, A. Ranjbari and E. Etiévant, *Int. J. Hydrogen Energy*, 2010, **35,** 5043-5052.
7 R. B. Levy and M. Boudart, *Science*, 1973, **181,** 547-549.
8 D. V. Esposito, S. T. Hunt, Y. C. Kimmel and J. G. Chen, *J. Am. Chem. Soc.*, 2012, **134,** 3025-3033.
9 S. Wirth, F. Harnisch, M. Weinmann and U. Schröder, *Appl. Catal. B-Env.*, 2012, **126**, 225-230.
10 F. Harnisch, U. Schröder, M. Quaas and F. Scholz, *Appl. Catal. B-Env.*, 2009, **87,** 63-69.
11 H. Tributsch and J. C. Bennett, *J. Electroanal. Chem.*, 1977, **81,** 97-111.
12 B. Hinnemann, P. G. Moses, J. Bonde, K. P. Jørgensen, J. H. Nielsen, S. Horch, I. Chorkendorff and J. K. Nørskov, *J. Am. Chem. Soc.*, 2005, **127,** 5308-5309.
13 J. Kibsgaard, Z. Chen, B. N. Reinecke and T. F. Jaramillo, *Nat. Mater.*, 2012, **11,** 963-969.
14 T. F. Jaramillo, K. P Jørgensen, J. Bonde, J. H. Nielsen, S. Horch and I. Chorkendorff, *Science*, 2007, **317,** 100-102.
15 D. Voiry, M. Salehi, R. Silva, T. Fujita, M. Chen, T. Asefa, V. B. Shenoy, G. Eda, M. Chhowalla, *Nano Lett.*, 2013, **13**, 6222-6227.
16 T.-W Lin, C.-J. Liu and J.-Y Lin,.*Appl. Catal. B-Env.*, 2013, **134-135,** 75-82.
17 Y. Li, H. Wang, L. Xie, Y. Liang, G. Hong and H. Dai, *J. Am. Chem. Soc.*, 2011, **133,** 7296-7299.
18 H. Vrubel and X. Hu, *Angew. Chem. Int. Ed.*, 2012, **51,** 12703-12706.
19 W.-F. Chen, C.-H. Wang, K. Sasaki, N. Marinkovic, W. Xu, J. T. Muckerman, Y. Zhu and R. R. Adzic *Energy Environ. Sci.*, 2013, **6,** 943-951.
20 W.-F. Chen, S. Iyer, K. Sasaki, C.-H. Wang, Y. Zhu, J. T. Muckerman and E. Fujita, *Energy Environ. Sci.*, 2013, **6,** 1818-1826.
21 W.-F. Chen, K. Sasaki, C. Ma, A. I. Frenkel, N. Marinkovic, J. T. Muckerman, Y. Zhu and R. R. Adzic *Angew. Chem. Int. Ed.*, 2012, **51,** 6131-6135.

22 A. T. Garcia-Esparza, D. Cha, Y. Ou, J. Kubota, K. Domen and K. Takanabe, *ChemSusChem* , 2013, **6,** 168.

23 S. Trasatti, *Electroanal. Chem. and Interf. Electrochem.*, 1972, **39,** 163-184.

24 P. R. Zabinski, H. Nemoto, S. Meguro, K. Asami. and K. Hashimoto, *J. Electrochem Soc.*, 2003, **150,** C717-C722.

25 E. Navarro-Flores, Z. Chong and S. Omanovic, *J. Mol. Catal. A: Chem* 2005, **226,** 179-197.

26 J. Perez, E. R. Gonzalez and H. M. Villullas, *J. Phys. Chem. B*, 1998, **102,** 10931-10935.

27 V. Briois, E. Fonda, S. Belin, L. Barthe, C. La Fontaine, F. Langlois, M. Ribbens and F. Villain, *UVX* , 2011, **2010,** 41-47.

28 A. Filipponi and A. Di Cicco, *Phys. Rev. B*, 1995, **52,** 15135−15149.

29 A. Filipponi, A. Di Cicco and C. R. Natoli, *Phys. Rev. B*, 1995, **52,** 15122−15134.

30 E. Proietti, F. Jaouen, M. Lefèvre, N. Larouche, J. Tian, J. Herranz and J.-P. Dodelet, *Nat. Commun.* 2011, **2,** 416.

31 C. L. Bull, T. Kawashima, P. F. McMillan, D. Machon, O. Shebanova, D. Daisenberger, E. Soignard, E. Takayama-Muromachi and L. C. Chapon, *J. Solid State Chem.*, 2006, **179,** 1762-1767.

32 T. Ressler, J. Wienold, R. E. Jentoft and T. Neisius, *J. Catal.*, 2002, **210,** 67-83.

33 F. D. Hardcastle and I. E. Wachs, *J. Raman Spectros.*, 1990, **21,** 683-691.

34 B. G. Demczyk, J. G. Choi and L. T. Thompson, *Appl. Surf. Sci.*, 1994, **78,** 63-69.

35 Z. B. Wei, Q. Xin, P. Grange and B. Delmon, *Solid State Ionics*, 1997, **101-103,** 761-767.

36 B. Cao, G. M. Veith, J. C. Neuefeind, R. R. Adzic and P. G. Khalifah,. *J. Am. Chem. Soc.*, 2013, **135,** 19186–19192.

37 F. Jaouen, S. Marcotte, J. P. Dodelet and G. Lindbergh, *J. Phys. Chem. B*, 2003, **107,** 1376-1386.

38 Z. B. Wei, P. Grange and B. Delmon, *Appl. Surf. Sci.*, 1998, **135,** 107-114.

39 B. L. Abrams, P. C. K. Vesborg, J. L. Bonde, T. F. Jaramillo and I. Chorkendorff, *J. Electrochem Soc.*, 2009, **156,** B273-B282.

40 S. Trasatti and O. A. Petrii, *Pure Appl. Chem.,* 1991*,* **63,** 711-734.

41 S. Fletcher, *J. Solid State Electrochem.*, 2009, **13,** 537-549.

42 J. O. M. Bockris, I. A. Ammar and K. M. S. Huq, *J. Phys. Chem.*, 1957, **61,** 879-886.

43 I. M. Kodintsev and S. Trasatti, *Electrochim. Acta*, 1994, **39,** 1803-1808.

44 J. Kim, S. Byun, A. J. Smith, J. Yu and J. Huang, *J. Phys. Chem. Lett.*, 2013, **4,** 1227-1232.

45 T. Wang, L. Liu, Z. Zhu, P. Papakonstantinou, J. Hu, H. Liu and M. Li,, *Energy Environ. Sci.*, 2013, **6,** 625-633.

46 J. Kibsgaard, T. F. Jaramillo and F. Besenbacher, *Nat. Chem.*, 2014, **6,** 248-253.